RSC Advances

PAPER

View Article Online
View Journal | View Issue

Cite this: *RSC Adv.*, 2025, **15**, 24975

$Ti_3C_2T_x$ MXenes and Mn_3O_4 nanoparticles synergistically promote the electrochemical synthesis of ammonia under ambient conditions†

Lanxiang Huang, *[ab] Renchuan Deng,[a] Xiang Wang, [a] Qin Wang[a] and Yuan Liang[a]

Received 13th March 2025
Accepted 26th June 2025

DOI: 10.1039/d5ra01799h

rsc.li/rsc-advances

Ammonia serves as a hydrogen energy carrier and a renewable, zero-carbon fuel alternative that is safely transportable. The electrochemical catalytic reduction of N_2 to NH_3 in aqueous electrolytes at ambient temperature and pressure (eNRR) using electricity generated from renewable energy sources such as solar and wind power can provide an environmentally friendly approach. To effectively suppress the occurrence of hydrogen evolution side reactions, it is necessary to design and synthesize catalysts with high selectivity for N_2 adsorption. Owing to the ability of transition metals with unoccupied d orbitals to significantly promote the adsorption of N_2 molecules and the activation of inert bonds, researchers have explored manganese-oxide catalysts through both experimental and theoretical studies. However, manganese oxides are semiconductor materials with poor conductivity. To solve this problem, the $Ti_3C_2T_x$ MXene material can be introduced as a carrier for manganese oxide particles. In this study, the $Ti_3C_2@Mn_3O_4$ composite was used as an electrocatalyst for ammonia synthesis under ambient conditions using a simple method. Benefiting from the synergistic catalytic effect of MXene and Mn_3O_4, the composite exhibits excellent catalytic performance for ammonia synthesis, with an NH_3 yield rate of 53.7 μg h^{-1} $mg_{cat.}^{-1}$ and satisfactory FE of 10.4% at −0.6 V (*vs.* RHE) under ambient conditions. The composite catalyst exhibits excellent stability, durability, and selectivity, with outstanding synergistic effects, surpassing most reported NRR electrocatalysts. This simple and versatile strategy may offer researchers inspiration for rationally designing highly efficient NRR electrocatalysts.

1. Introduction

Ammonia is a hydrogen energy carrier that can be easily and safely transported, as well as a renewable and zero-carbon fuel. However, the Haber–Bosch process for producing ammonia is a high-temperature, high-pressure process with high energy consumption in the chemical industry, consuming about 2% of the world's energy annually. At the same time, the H_2 required for the reaction is mainly produced through the steam reforming of natural gas, with the required energy mainly derived from fossil fuels, resulting in annual CO_2 emissions of approximately 320 million tons.[1] Therefore, finding a green, environmentally friendly, and energy-efficient method for ammonia synthesis is of great significance for the sustainable development of the economy and ecology.

The electrochemical catalytic reduction of N_2 in aqueous electrolytes under ambient conditions to synthesize ammonia (eNRR), utilizing electricity generated from renewable energy sources such as solar and wind power, can provide an alternative and environmentally benign method. This method not only overcomes the limitations of thermodynamic equilibrium for the thermodynamically unfavorable NH_3 synthesis reaction with the driving force of electricity but also eliminates or reduces the constraints of thermodynamic equilibrium, thereby avoiding the reliance on temperature and high pressure conditions and reducing CO_2 emissions, becoming a highly researched field.[2–4] In acidic aqueous electrolytes, the reaction occurring at the cathode is[5]

$$N_2\,(g) + 6H^+\,(aq.) + 6e^- \rightarrow 2NH_3\,(g)\ (E^0 = 0.0577\ \text{V}\ vs.\ \text{SHE}) \quad (1)$$

At the same time, a side reaction occurs:

$$2H^+\,(aq.) + 2e^- \rightarrow H_2\,(g)\ (E^0 = 0\ \text{V}\ vs.\ \text{SHE}) \quad (2)$$

During the eNRR process, N_2 molecules need to be adsorbed and activated on the catalyst surface, followed by hydrogenation reactions. N_2 molecules are highly inert, so active H^+ ions are more easily adsorbed onto the catalyst surface, leading to strong competitive hydrogen evolution reactions (HER), with low

---

[a] *School of New Energy Materials and Chemistry, Leshan Normal University, Leshan, Sichuan, 614000, China. E-mail: 120678486@qq.com*

[b] *West Silicon Photovoltaic New Energy Industry Technology Research Institute, Leshan, Sichuan, 614000, China*

† Electronic supplementary information (ESI) available. See DOI: **https://doi.org/10.1039/d5ra01799h**

faradaic efficiency (FE) for eNRR and slow ammonia synthesis rates.[6,7] Therefore, suppressing the hydrogen evolution reaction is key to improving the performance of eNRR.

To effectively suppress the occurrence of hydrogen evolution side reactions, it is necessary to design and prepare a catalyst with high selectivity for N_2 adsorption. In light of the fact that transition metals with unoccupied d orbitals can significantly promote the adsorption of N_2 molecules and the activation of inert bonds, researchers have explored manganese-based catalysts through experimental and theoretical studies.[8–11] Kong *et al.* used MnO_2 as an NRR electrocatalyst and achieved an NH_3 yield rate of 34.12 μg h^{-1} $mg_{cat.}^{-1}$ in 0.1 M HCl;[12] Wu *et al.* synthesized Mn_3O_4 nanocubes as an NRR electrocatalyst with an NH_3 yield rate of 11.6 μg h^{-1} $mg_{cat.}^{-1}$ and FE of 3.0% in 0.1 M Na_2SO_4;[13] Zheng *et al.* reported a MnO-based composite, which displayed a low FE of 1.5% in 0.1 M Na_2SO_4.[14]

As a transition metal oxide, manganese oxides are semiconductor materials with poor conductivity. In order to improve its conductivity, the $Ti_3C_2T_x$ MXene material can be introduced as a carrier for manganese oxide particles. MXenes ($M_{n+1}X_n$, $n =$ 1, 2, and 3)are 2D layered transition metal carbides and nitrides that exhibit excellent conductivity, good hydrophilicity, and a variety of surface terminal groups (T_x, such as =O, –OH, and –F).[15–17] The synthesized manganese oxide nanoparticles can be firmly anchored on the surface and interlayers of $Ti_3C_2T_x$ MXene materials due to the electronegativity of the surface terminals (T_x). In addition, recent research suggests that $Ti_3C_2T_x$ exhibits good NRR activity.[18–21]

In this study, a Ti_3C_2@Mn_3O_4 composite was used as an electrocatalyst for ammonia synthesis under ambient conditions in a simple method. Benefiting from the synergistic catalytic effect of MXene and Mn_3O_4, the composite exhibits excellent catalytic performance for ammonia synthesis with an NH_3 yield rate of 53.7 μg h^{-1} $mg_{cat.}^{-1}$ and satisfactory FE of 10.4% at −0.6 V (*vs.* RHE) under ambient conditions. The composite catalyst exhibits excellent stability, durability, and selectivity, with outstanding synergistic effects, surpassing most reported NRR electrocatalysts. This simple and versatile strategy may offer researchers inspiration for rationally designing highly efficient NRR electrocatalysts.

2. Experimental section

2.1 Material preparation

First, an appropriate amount of Ti_3AlC_2 MAX material was weighed and etched with hydrofluoric acid (HF) to remove the Al layer. The mixture was then filtered, washed, and vacuum dried to obtain the layered $Ti_3C_2T_x$ MXene material.[22] Subsequently, 0.1 g of $Ti_3C_2T_x$ MXenes was ultrasonically dispersed in 50 mL of deionized water until a uniform dispersion was formed, followed by the addition of 15 mL of a $MnSO_4$ solution (0.05 g mL^{-1}) into the dispersion with continuous stirring. Due to the abundant terminal groups (T_x, such as O, –F, and –OH) of $Ti_3C_2T_x$ MXene and electronegativity, positively charged manganese ions (Mn^{2+}) will be electrostatically attracted to intercalate between the $Ti_3C_2T_x$ MXene layers and firmly adsorb on its surface; meanwhile, the intercalation of manganese ions will effectively increase the interlayer spacing of $Ti_3C_2T_x$ MXenes.[23]

Then, 10 mL of KOH solution with a concentration of 0.2 g mL^{-1} was added dropwise to the dispersion under continuous stirring for 30 min. The added hydroxide ions (OH^-) reacted with Mn^{2+} to form manganese hydroxide ($Mn(OH)_2$), which was immediately oxidized to manganese tetroxide (Mn_3O_4) in the air atmosphere. The resulting Mn_3O_4 was firmly anchored to the surface of the $Ti_3C_2T_x$ MXene material to form the Ti_3C_2@Mn_3O_4 composite materials, thereby preventing further growth of Mn_3O_4 nanoparticles. The resulting dispersion was vacuum-filtered and washed until the pH was 7–8, then dried under vacuum at 100 °C for 12 h. After cooling to room temperature, the material was used for electrode preparation. At the same time, pure Mn_3O_4 particles were synthesized using the same method for comparative experiments.

2.2 Material characterization

The phase structure of the prepared materials was characterized using an X-ray diffractometer (XRD, DX-600X, Cu-Kα1). The surface elemental composition and the corresponding chemical structure of the prepared materials were analyzed using an X-ray photoelectron spectrometer (XPS, Thermo Scientific NEXSA, Al-Kα). The micro-morphology of the materials was observed using a field emission scanning electron microscope (SEM, FEI Inspect F50), transmission electron microscope (TEM), and high-resolution transmission electron microscope (HRTEM, JEM2100). The manganese (Mn) content in the Ti_3C_2@Mn_3O_4 composite material was analyzed using an inductively coupled plasma emission spectrometer (ICP-OES, AGILENT 730).

2.3 Electrochemical analysis

The electrochemical tests were conducted in a two-compartment electrolytic cell, separated by a Nafion membrane. A platinum electrode and saturated Hg/Hg_2SO_4 electrode were applied as the counter electrode and reference electrode, respectively. For the working electrode, an appropriate amount of catalyst and Nafion solution (5 wt%) were ultrasonically dispersed in a mixed solution of pure water and anhydrous ethanol to form a uniform dispersion. Then, a small amount of the dispersion was loaded onto a carbon cloth with an area of 1 × 1 cm^2. The final catalyst loading is about 0.5 mg cm^{-2}. The electrolysis cell (H_2SO_4, pH = 2) was continuously purged with high-purity N_2 for 30 min under sealed conditions to exclude air while ensuring that the N_2 was saturated. The corresponding electrochemical tests were performed at room temperature and atmospheric pressure using an electrochemical workstation. All electrode potentials were converted to those corresponding to the reversible hydrogen electrode (E (*vs.* RHE) = E (*vs.* Hg/Hg_2SO_4) + 0.616 + 0.059 × pH).

The linear sweep voltammetry (LSV) curves were determined at a scan rate of 5 mV s^{-1} and the corresponding chronoamperometry tests were carried out at a series of negative potentials. Throughout the experiment, a continuous flow of high-purity nitrogen gas was maintained to the cathodic compartment. Cyclic voltammetry (CV) curves were conducted in the range of 0.35 and 0.45 V with the scan rates of 20, 40, 60, 80, and 100 mV s^{-1}.

2.4 Determination of NH_3

The yield of ammonia (NH_3) produced by the electrocatalytic reduction of N_2 was determined using the indophenol blue method.[24,25] 4 mL of the electrolyte after the reaction was mixed with 500 μL of sodium salicylate ($C_7H_5NaO_3$) solution (0.4 M $C_7H_5NaO_3$, 0.32 M NaOH), 50 μL of sodium hypochlorite (NaClO) solution (0.05 M NaClO, 0.75 M NaOH), and 50 μL of sodium nitroprusside ($C_5FeN_6Na_2O$) solution (1 wt%). The mixed solution was then kept in the dark for 2 h. Then, the absorbance of the mixed solution was measured using a UV-visible spectrophotometer. The concentration–absorbance curve was plotted using a standard NH_4Cl solution of 0∼2 μg mL^{-1}. The yield of ammonia was calculated using eqn (3):

$$r_{NH_3} = (c_{NH_3}V)/(tm) \tag{3}$$

where c_{NH_3} is the measured concentration of ammonia (μg mL^{-1}), V is the volume of the electrolyte (mL), t is the reaction time (h), and m is the amount of catalyst used (mg).

2.5 Determination of N_2H_4

The Watt–Chrisp method was used for hydrazine detection.[24,25] First, *p*-dimethylaminobenzaldehyde (0.998 g) was dissolved in ethanol (50 mL) to act as the colorimetric reagent. Then, the electrolyte (2 mL) was thoroughly mixed with the colorimetric reagent (2 mL) for 20 min, and the absorbance was detected using a UV-visible spectrophotometer (λ = 455 nm). The absorbance curve was plotted using standard hydrazine solutions (0–1 μg mL^{-1}).

2.6 FE of NH_3 production

The FE for ammonia synthesis is the ratio of the charge transferred for ammonia production to the total consumed charge, which is given by eqn (4):

$$\mathrm{FE} = 3Fn_{NH_3}/Q \tag{4}$$

F is the Faraday constant (96 485 C mol^{-1}), n_{NH3} is the molar amount of produced ammonia (mol), and Q is the total consumed charge (C).

3. Results and discussions

3.1 Morphology and structure

Fig. 1a shows the XRD patterns of the samples. When Mn_3O_4 nanoparticles were *in situ* grown on the surface of $Ti_3C_2T_x$ MXene layers to form the $Ti_3C_2@Mn_3O_4$ composites, the original XRD characteristic peak at 8.85° shifted to a lower angle at 6.9°, and the interlayer spacing of $Ti_3C_2T_x$ MXene increased from 0.998 to 1.280 nm, indicating manganese ions were effectively intercalated into the $Ti_3C_2T_x$ MXene layers; the diffraction peaks at 18.0°, 2.9°, 32.3°, 36.1°, 36.4°, 44.4°, 59.8° matched with the standard card of Mn_3O_4 (PDF# 24-0734), corresponding to the diffraction peaks of (1 0 1), (1 1 2), (1 0 3), (2 1 1), (2 02), (2 2 0), and (2 2 4), respectively. The ICP-OES analysis revealed that the manganese content in $Ti_3C_2@Mn_3O_4$ was 0.456 g, and thus the calculated content of Mn_3O_4 in the $Ti_3C_2@Mn_3O_4$ composite was 63.3%. Fig. 1b–f show the XPS spectra of the $Ti_3C_2@Mn_3O_4$ material. The Ti2p spectrum (Fig. 1c) exhibits three sets of resolved peaks at 455.3 and 461.0, 456.8 and 462.4, 458.6 and 464.2 eV, corresponding to Ti–C, Ti^{3+}, and Ti^{4+}(Ti–O),[23] respectively. The C 1 s spectrum (Fig. 1d) can be deconvoluted into four Gaussian peaks, with the strongest peak at 284.8 eV corresponding to the C–C bonds, while the other peaks at 285.2, 286.4 and 288.3 eV correspond to the C–Ti, C–O and C–F bonds, respectively.[23] As for Mn 3s (Fig. 1e), the peaks at 83.2 and 88.9 eV correspond to Mn $3s_{3/2}$ and Mn $3s_{1/2}$, respectively, and the binding energy difference (ΔE) between these two peaks is 5.7 eV, which is lower than that of Mn^{2+} ($\Delta E =$ 6 eV) and higher than that of Mn^{3+} ($\Delta E = 5.3$ eV), indicating that the valence state of Mn in the $Ti_3C_2@Mn_3O_4$ composites is a mixed valence state of Mn^{2+} and Mn^{3+}.[26] The O 1s spectrum (Fig. 1f) can be deconvoluted into three peaks at 529.7, 530.1, and 531.4 eV, corresponding to O–C, Mn–O–Mn (Ti–O), and O–H,[26] respectively. All the above analysis indicates that the prepared $Ti_3C_2T_x$ MXene materials indeed have rich surface termination structures, such as =O, –OH, and –F, thereby endowing $Ti_3C_2T_x$ MXenes with electronegativity.

The acid treatment (Fig. 2a and b) results in the etching of Al, yielding $Ti_3C_2T_x$ MXenes with a smooth accordion-like surface and a significantly increased layer spacing. The prepared $Ti_3C_2@Mn_3O_4$ composites were observed and analyzed using TEM and HRTEM. As can be seen Fig. 2c and d, due to the strong electrostatic attraction between the surface terminals T_x (=O, –F, and –OH) of $Ti_3C_2T_x$ MXenes and Mn^{2+}, Mn^{2+} will be inserted into the interlayer of $Ti_3C_2T_x$ MXenes and adsorbed on its surface, thus anchoring the generated Mn_3O_4 particles firmly in the interlayer and on the surface of $Ti_3C_2T_x$ MXenes, inhibiting their growth or aggregation into secondary large particles. Meanwhile, the presence of interlayer Mn_3O_4 nanoparticles can effectively expand the interlayer spacing of $Ti_3C_2T_x$ MXenes, which increased from 0.998 to 1.280 nm, as revealed by the aforementioned XRD (Fig. 1a). The planar spacings of the generated nanoparticles are 0.313, 0.294, and 0.254 nm, corresponding to the (1 1 2), (2 0 0), and (2 1 1) planes of Mn_3O_4, respectively, analyzed by HRTEM (Fig. 2d). Meanwhile, the laminar structure of $Ti_3C_2T_x$ MXenes can be clearly seen. The distributions of Mn, O, Ti, and C in the $Ti_3C_2@Mn_3O_4$ composites are shown in Fig. 2e, indicating these elements are uniformly dispersed in the material. This result demonstrates that Mn_3O_4 nanoparticles are evenly grown on $Ti_3C_2T_x$ MXenes.

3.2 Electrocatalytic performance

Firstly, the linear sweep voltammetry (LSV) curves were determined to evaluate the NRR activity of $Ti_3C_2@Mn_3O_4$ in N_2- and Ar-saturated H_2SO_4 solutions (pH = 2) (tests confirm that neither Ar nor N_2 contained any other nitrogen species (Table S1†)). As shown in Fig. 3a, the two curves of the catalyst under N_2 and Ar conditions exhibit similar trends but different current

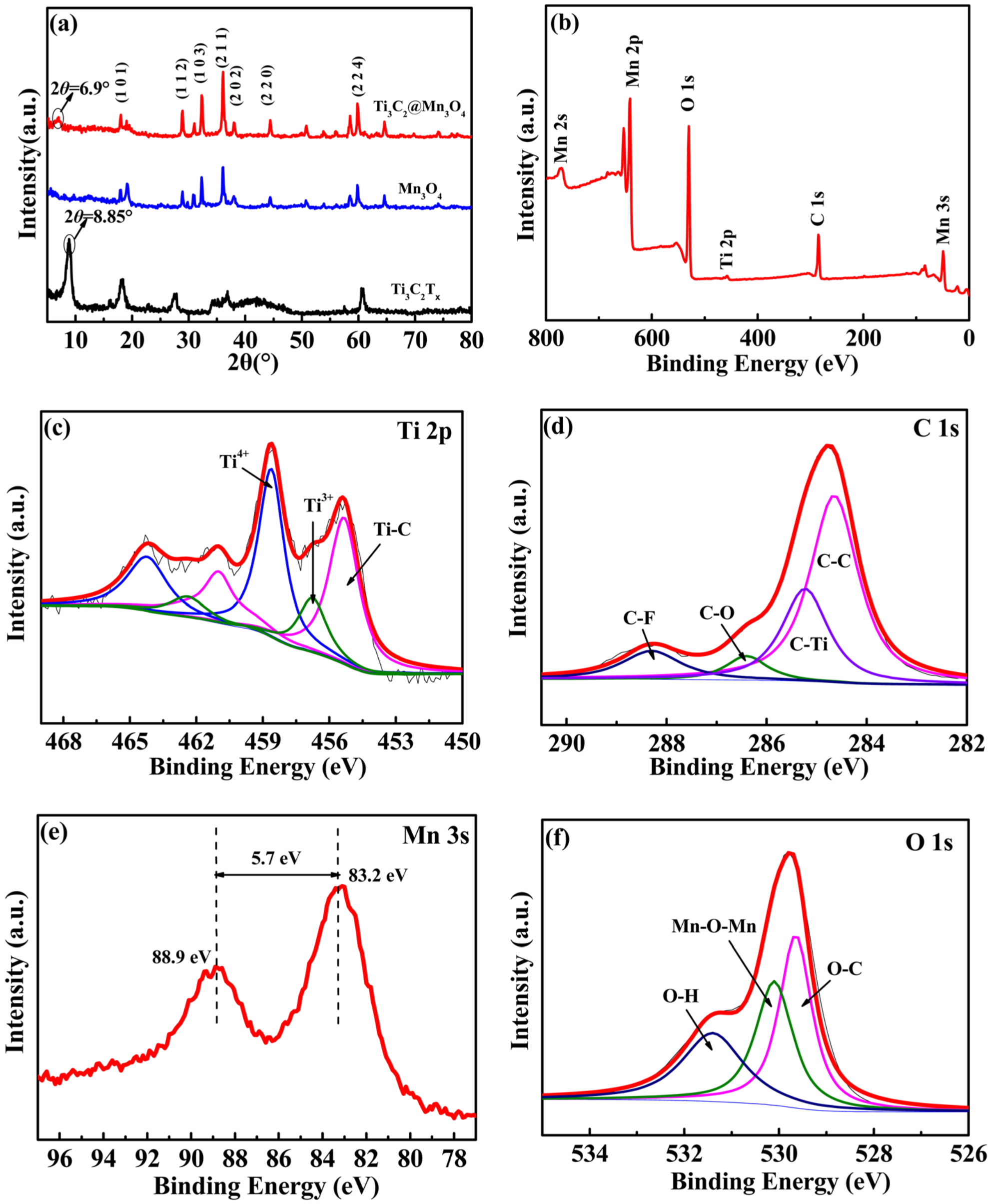

Fig. 1 XRD patterns of (a) $Ti_3C_2T_x$ MXenes, Mn_3O_4 and $Ti_3C_2@Mn_3O_4$; (b) overall survey, (c) Ti 2p, (d) C 1s, (e) Mn 3s, and (f) O 1s XPS spectra of $Ti_3C_2@Mn_3O_4$.

densities. Apparently, at the same voltage, the current density is higher in N_2 atmosphere, indicating a more active NRR reaction. In general, the more negative the voltage, the more pronounced the reduction reaction. However, based on the competitive hydrogen evolution side reaction of the NRR reaction, the hydrogen evolution becomes more intense as the voltage increases, leading to a gradual decrease in FE. To further evaluate the HER activity of $Ti_3C_2@Mn_3O_4$, the LSV curve of the carbon cloth without the electrocatalyst was determined under an Ar atmosphere as a control experiment. The current density with the catalyst is higher than that of carbon cloth at the same potential, indicating that the catalyst possesses HER catalytic activity. The corresponding Tafel analysis is presented in Fig. 3b.

In acidic electrolytes, the HER process primarily involves three steps: electrochemical hydrogen adsorption (Volmer step), electrochemical desorption (Heyrovsky step), and chemical desorption (Tafel step), as shown in the following equations:[27]

$$\text{Volmer: } H_3O^+ + e^- \rightarrow H_{ads} + H_2O \text{ (120 mV dec}^{-1}\text{)} \quad (5)$$

$$\text{Heyrovsky: } H_{ads} + H_3O^+ + e^- \rightarrow H_2 + H_2O \text{ (40 mV dec}^{-1}\text{)} \quad (6)$$

$$\text{Tafel: } 2H_{ads} \rightarrow H_2 \text{ (30 mV dec}^{-1}\text{)} \quad (7)$$

H_3O^+ combines with electrons on the catalyst surface to readily form H_{ads}, which constitutes the Volmer step, with a Tafel slope of 120 mV dec^{-1}. Subsequently, the generated H_{ads}

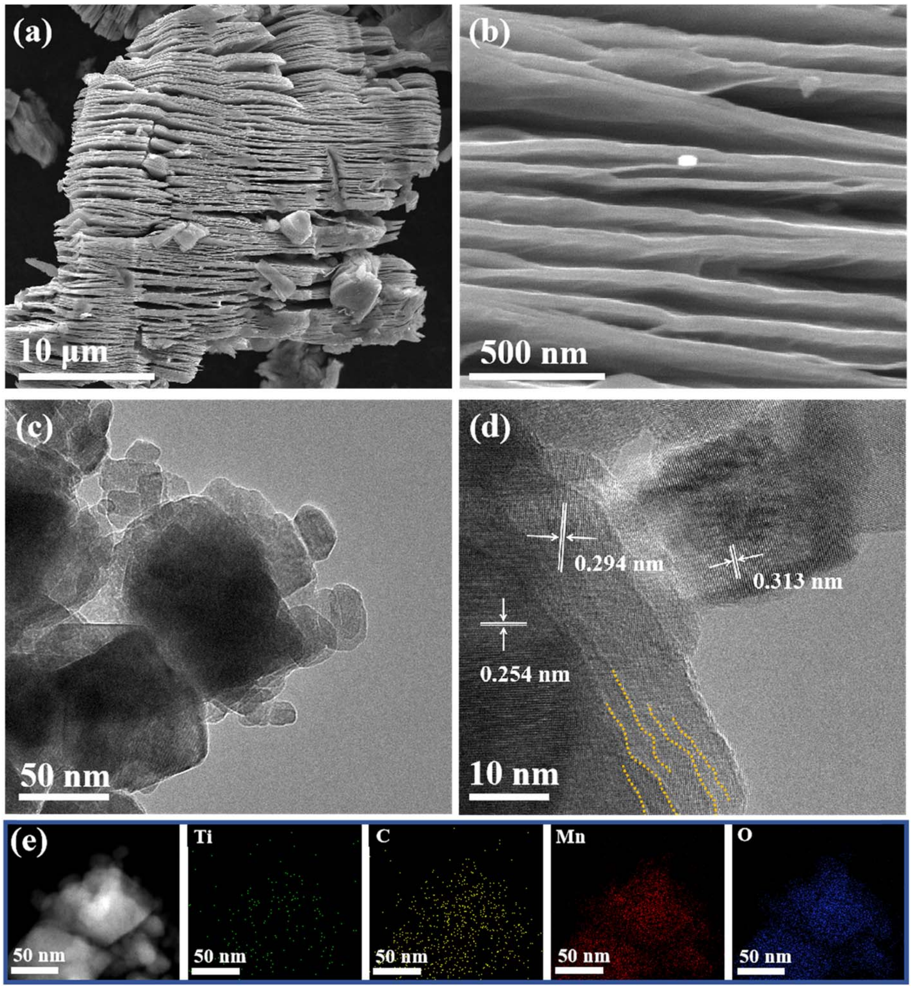

Fig. 2 (a) and (b) SEM images of $Ti_3C_2T_x$ MXenes; TEM (c) and HRTEM (d) images of $Ti_3C_2@Mn_3O_4$; (e) corresponding elemental mappings of Mn, O, Ti, and C.

may follow two distinct pathways: The adsorbed H_{ads} combines with another H_3O^+ and gains an electron to form H_2, which then desorbs from the active site (Heyrovsky step), with a Tafel slope of 40 mV dec^{-1}. Alternatively, two adjacent H_{ads} species directly combine to produce H_2, followed by desorption (Tafel step), with a Tafel slope of 30 mV dec^{-1}. Tafel slope serves as a crucial indicator of the kinetics in electrochemical reactions, particularly in HER. Notably, under an argon atmosphere, the Tafel slope recorded with just a carbon cloth or in the presence of the catalyst is 188 and 153 mV dec^{-1}, respectively. Both values significantly exceed the 120 mV dec^{-1} threshold, strongly suggesting that the Volmer step serves as the rate-determining step in the HER mechanism.

In order to determine the optimal working voltage for the NRR reaction, a series of NRR experiments were carried out using the comparative potentials of −0.4 to −0.80 V, and the resulting time-dependent current density curves are shown in Fig. 3c. The UV-vis absorption spectrum of the electrolytes after 2 h of electrocatalysis (Fig. 3d) shows an obvious absorption, which proves the NRR catalytic performance of $Ti_3C_2@Mn_3O_4$. With the increase in voltage, the absorption peak intensity shows a trend of first increasing and then decreasing, with the strongest peak at −0.6 V. The yield of ammonia tested by the indophenol method (Fig. S1†) also shows a trend of first increasing and then decreasing with the rise in voltage, with the highest yield (53.7 μg h^{-1} mg$_{cat.}$$^{-1}$) at −0.6 V, while FE shows a gradually declining trend (Fig. 3e). Although a high FE is observed at −0.4 V, the NH_3 yield rate is too low; therefore, −0.6 V was chosen as the optimal operating voltage, at which the highest ammonia production rate was obtained and the FE was also high (10.4%). Hydrazine (N_2H_2) is a potential secondary product in the electrocatalytic NRR process, which was barely detected by the Watt and Crisp methods (Fig. S2 and S3†).

Subsequently, isotopic labeling measurements with $^{14}N_2$ and $^{15}N_2$ gas feeds were conducted to confirm the true source of NH_3. $^{14}N_2$ exhibits a reaction duration of 6 hours (h), whereas $^{15}N_2$ completes the same process within 2 h. The results (Fig. 3f) of the ^{1}H-NMR spectrum display the characteristic triplet and doublet peaks of $^{14}NH_4^+$ and $^{15}NH_4^+$, corresponding to the used $^{14}N_2$ and $^{15}N_2$ gas feeds, respectively.[28–30] This indicates that the nitrogen in the ammonia indeed comes from the nitrogen gas

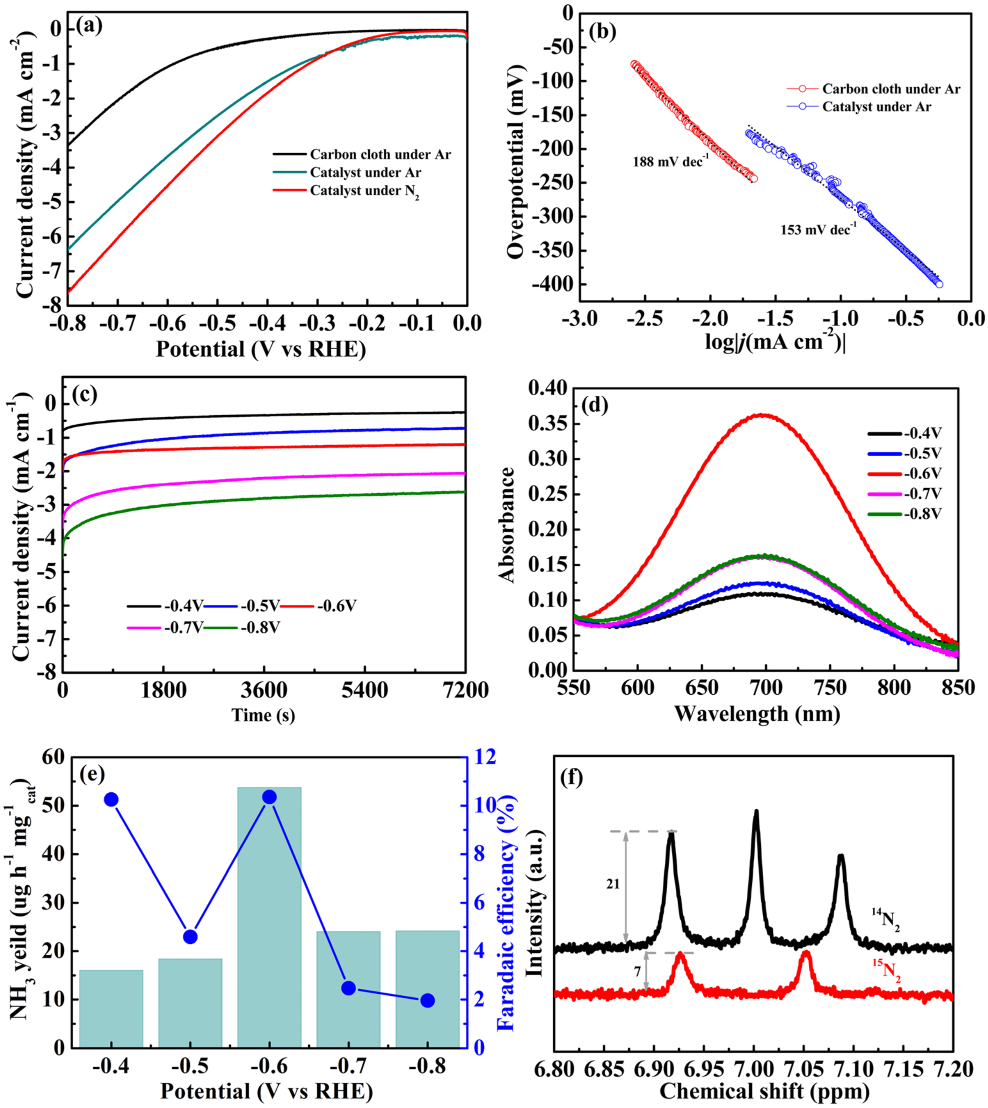

Fig. 3 (a) LSV curves in N_2- and Ar-saturated solutions. (b) Tafel slope with carbon cloth alone and in the presence of a catalyst. (c) Chronoamperometry results at the corresponding potentials. (d) UV-vis absorption spectra of electrolytes stained with indophenol indicator for 2 h. (e) NH_3 yield rate and FEs for $Ti_3C_2@Mn_3O_4$ at the corresponding potentials. (f) ^{1}H-NMR spectra of the electrolyte after electroreduction under $^{14}N_2$ (6 h) and $^{15}N_2$ (2 h) feed gases.

used. As evidenced by the ^{1}H-NMR spectrum analysis, the nitrogen isotopic composition exhibits a distinct temporal pattern with the $^{14}N_2$ peak intensity (21 a.u.) demonstrating a three-fold enhancement compared to the $^{15}N_2$ counterpart (7 a.u.). This proportional relationship aligns with the temporal progression of the reaction, providing quantitative evidence for the time-dependent accumulation of ammonia products.

In order to verify that N_2 is the main nitrogen source for the ammonia synthesis reaction, the following comparative experiments were conducted. (i) The $Ti_3C_2@Mn_3O_4$ catalyst was electrolyzed at the open-circuit voltage in a N_2-saturated electrolyte for 2 h. (ii) The black CP was electrolyzed at −0.6 V in a N_2-saturated electrolyte for 2 h. (iii) The $Ti_3C_2@Mn_3O_4$ catalyst was electrolyzed at −0.6 V in an Ar-saturated electrolyte for 2 h. The UV-vis absorption spectra of the electrolytes obtained from the above three comparisons, treated with indophenol indicator, are shown in Fig. 4a, which shows that only a slight amount of NH_3 was detected in cases (i), (ii), and (iii) compared to $Ti_3C_2@Mn_3O_4$, indicating that electrocatalytic NRR occurs only under a N_2-saturated atmosphere and a specific applied voltage. The durability and stability of catalysts are also important indicators for evaluating the performance of electrocatalysts. Fig. 4b shows the NH_3 yield rates and corresponding FEs of $Ti_3C_2@Mn_3O_4$ with alternating 2 h-cycles in N_2-saturated electrolytes (Fig. S4†). As can be seen, during the 8 cycles of intermittent operation, the NH_3 yield rates remained largely unchanged despite minor fluctuations and the corresponding FEs also remained nearly stable. The NH_3 yield rates and corresponding FEs of the $Ti_3C_2@Mn_3O_4$ composite material during alternating 2 hour cycles in N_2- and Ar-saturated electrolytes, respectively, are shown in Fig. 4c and S5.† In the N_2 atmosphere, the NH_3 yield rate remained stable at

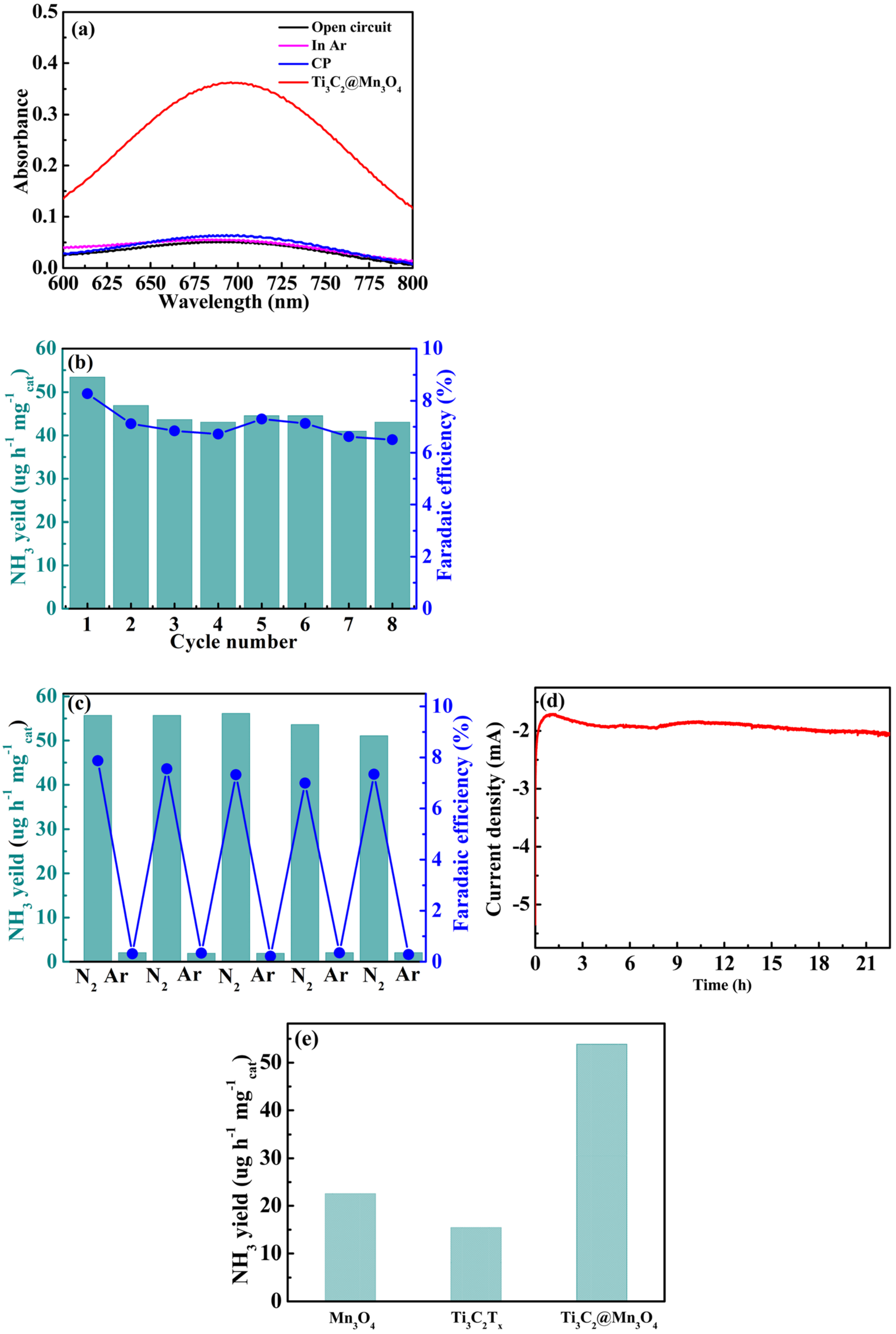

Fig. 4 (a) UV-vis absorption spectra of the electrolyte after charging at −0.6 V for 2 h under different electrochemical conditions. (b) NH_3 yield rate and the corresponding FEs of $Ti_3C_2@Mn_3O_4$ with alternating 2 h cycles in the N_2-saturated electrolytes. (c) NH_3 yield rate and the corresponding FEs of $Ti_3C_2@Mn_3O_4$ with alternating 2 h cycles in N_2- and Ar-saturated electrolytes. (d) Time-dependent current density curve for the $Ti_3C_2@Mn_3O_4$ catalyst at −0.6 V for 22 h. (e) NH_3 yield of Mn_3O_4, $Ti_3C_2T_x$ and $Ti_3C_2@Mn_3O_4$.

approximately 55 μg h^{-1} $mg_{cat.}{}^{-1}$, with the FE maintained at around 7%. In contrast, under an Ar atmosphere, the detected NH_3 yield was negligible (∼2 μg h^{-1} $mg_{cat.}{}^{-1}$), and the FE was essentially 0% due to no appreciable NH_3 production. These results demonstrate that the catalyst shows effective catalytic performance for eNRR under ambient conditions. After a long cycle of 22 h (Fig. 4d), there was no significant difference in the current density of catalysis at an applied potential of −0.6 V. Moreover, the XRD patterns of the electrode before and after cycling are identical (Fig. S6†). The excellent catalytic

Table 1 Comparison with other literature

Materials	Optimal operating voltage (V *vs.* RHE)	NH_3 yield rate (ug h^{-1} $mg_{cat.}^{-1}$)	FE (%)	References
	−0.6	53.7	10.4	This work
SnS_2	−0.5	3.3	10.8	8
MnO_2-$Ti_3C_2T_x$	−0.55	34.1	11.3	12
Mn_3O_4 nanocube	−0.8	11.6	3	13
MnO-carbon nanofibers	−1.25	35.9	1.5	14
$Ti_3C_2T_x$ MXene nanosheets	−0.4	20.4	9.3	20
Fluorine-free $Ti_3C_2T_x$ nanosheets	−0.3	36.9	9.1	21
Mn_3O_4 nanoparticles	−0.5	25.9	5.5	31
CuAg/Ti_3C_2	−0.5	4.1	9.7	32
Molybdenum carbide	−0.5	7.7	1.8	33
Pd films grown on Ni foam	−0.1	18.2	10.3	34
SnO_2	−0.6	25.2	11.4	35
BiOCl-modified 2D titanium carbide MXene	−0.1	4.0	11.9	36
1T/2H mixed-phase MoSSe	−0.45	32.3	12.6	37
Gold nanoparticles	−0.3	23.0	73.3	38
Fe_{SA}–N–C	0	7.4	56.5	39

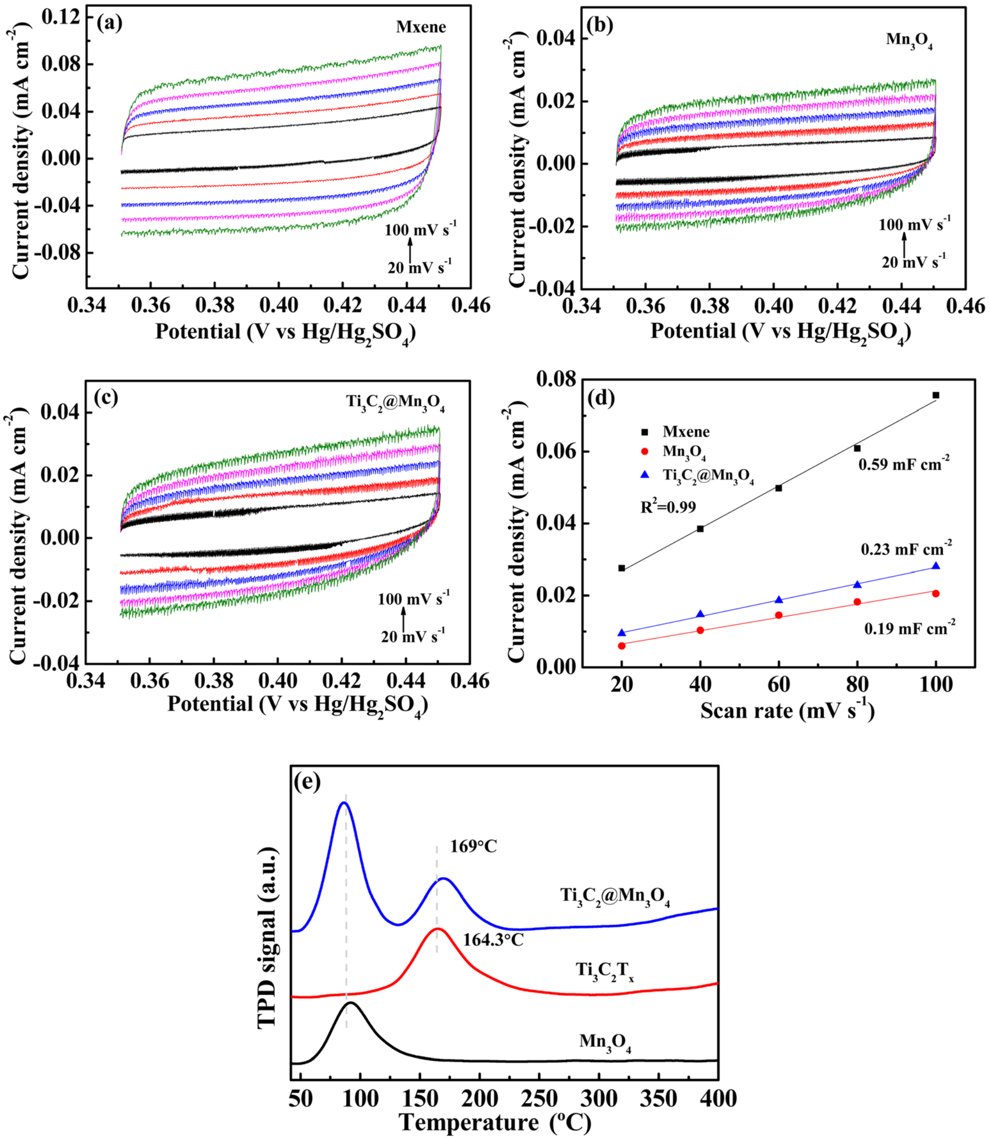

Fig. 5 (a) and (b), and (c) CV curves of different catalysts at various scan rates (20–100 mV s^{-1}) in the region of 0.35 to 0.45 V *vs.* Hg/Hg_2SO_4; (d) capacitive current densities at 0.40 V *vs.* Hg/Hg_2SO_4 as a function of scan rate for different catalysts. Slopes ($2C_{dl}$) were used to calculate the ECSA. (e) N_2-TPD profiles for Mn_3O_4, $Ti_3C_2T_x$ and $Ti_3C_2@Mn_3O_4$.

performance of the $Ti_3C_2@Mn_3O_4$ material is attributed to the synergistic catalytic effect of Mn_3O_4 and MXenes, as evident from Fig. 4e and S7.† The amount of ammonia produced at the Mn_3O_4, Ti_3C_2 and $Ti_3C_2@Mn_3O_4$ electrodes after electrolysis for 2 h under ambient conditions at −0.6 V is 22.5, 15.4 and 53.7 μg h^{-1} $mg_{cat.}^{-1}$, respectively.

As summarized in Table 1, the present work demonstrates superior NH_3 yield and FE compared with state-of-the-art electrocatalysts reported in the literature. Although ref. 38 demonstrates a high FE of 73.3%, it employs the noble metal gold as the catalyst and achieves only a modest NH_3 yield of 23 μg h^{-1} $mg_{cat.}^{-1}$. Similarly, ref. 39 reports an FE of 56.5%, but with a considerably lower NH_3 yield of merely 7.4 μg h^{-1} $mg_{cat.}^{-1}$. In comparison, our work achieves a superior NH_3 yield of 53.7 μg h^{-1} $mg_{cat.}^{-1}$ while maintaining competitive FE performance.

To understand the intrinsic advantages of $Ti_3C_2@Mn_3O_4$ for NRR catalytic activity, the electrochemical active surface area was estimated by the double-layer capacitance (C_{dl}) from CV experiments in the range of 0.35–0.45 V (Fig. 5a–c). The C_{dl} value of $Ti_3C_2T_x$ is calculated to be 0.59 mF cm^{-2} (Fig. 5d), which is larger than that of Mn_3O_4 (0.19 mF cm^{-2}), and the value of $Ti_3C_2@Mn_3O_4$ is calculated to be 0.23 mF cm^{-2}. As revealed from this data, the high specific surface area of MXene and its interaction with Mn_3O_4 can indeed effectively increase the electrochemical surface area of Mn_3O_4, thereby improving its catalytic activity. In order to investigate the intrinsic reason for the high electrocatalytic performance of $Ti_3C_2@Mn_3O_4$, N_2 temperature-programmed desorption (N_2-TPD) experiments were carried out, and the results are displayed in Fig. 5e. The chemical desorption peaks of Mn_3O_4 and Ti_3C_2 were located at 90 °C and 164 °C, respectively, in the N_2-TPD spectra. As for $Ti_3C_2@Mn_3O_4$, there were two characteristic peaks at around 90 °C and 169 °C, which are associated with the peak for the chemical adsorption of nitrogen for Mn_3O_4 and Ti_3C_2, respectively. This additionally confirms that the synergistic effect of Mn_3O_4 and Ti_3C_2 promoted the NRR catalytic performance of the $Ti_3C_2@Mn_3O_4$ material.

4. Conclusion

The $Ti_3C_2@Mn_3O_4$ composite was used as an electrocatalyst for ammonia synthesis under ambient conditions *via* a very simple method. Benefiting from the synergistic catalytic effect of MXenes and Mn_3O_4, the composite exhibits excellent catalytic performance for ammonia synthesis with an NH_3 yield rate of 53.7 μg h^{-1} $mg_{cat.}^{-1}$ and satisfactory FE of 10.4% at −0.6 V under ambient conditions. The composite catalyst exhibits excellent stability, durability, and selectivity, with outstanding synergistic effects, surpassing most reported NRR electrocatalysts. This simple and versatile strategy may offer researchers inspiration for rationally designing highly efficient NRR electrocatalysts.

Data availability

All data included in this study are available from the corresponding author upon request.

Conflicts of interest

There are no conflicts to declare.

Acknowledgements

The research was supported by the Sichuan Science and Technology Program (2024NSFSC0236).

References

1 G. Soloveichik, Electrochemical synthesis of ammonia as a potential alternative to the Haber–Bosch process, *Nat. Catal.*, 2019, **2**, 377–380.

2 X. W. Lv, Y. Liu, R. Hao, W. Tian and Z. Y. Yuan, Urchin-like Al-doped Co_3O_4 nanospheres rich in surface oxygen vacancies enable efficient ammonia electrosynthesis, *ACS Appl. Mater. Interfaces*, 2020, **12**, 17502–17508.

3 X. He, H. Guo, T. Liao, Y. Pu, L. Lai, Z. Wang and H. Tang, Electrochemically synthesized SnO_2 with tunable oxygen vacancies for efficient electrocatalytic nitrogen fixation, *Nanoscale*, 2021, **13**, 16307–16315.

4 Y. Zha, M. Liu, J. Wang, J. Feng, D. Li, D. Zhao, S. Zhang and T. Shi, Electrochemical ammonia synthesis by reduction of nitrate on Au doped Cu nanowires, *RSC Adv.*, 2023, **13**, 9839–9844.

5 H. Shen, C. Choi, J. Masa, X. Li, J. Qiu, Y. Jung and Z. Sun, Electrochemical ammonia synthesis: mechanistic understanding and catalyst design, *Chem*, 2021, **7**, 1–47.

6 P. Huang, Z. Cheng, L. Zeng, J. Yu, L. Tan, P. Mohapatra, L. Fan and Y. Zhu, Enhancing nitrogen electroreduction to ammonia by doping chlorine on reduced graphene oxide, *ACS Catal.*, 2020, **10**, 14928–14935.

7 G. Y. Arif, L. Luo, W. Ye, M. A. Mushtaq, X. Fang, X. Xiang, S. Jia and D. Yan, Hierarchical hollow nanotubes of NiFeV-layered double hydroxides@CoVP heterostructures towards efficient, pH-universal electrocatalytical nitrogen reduction reaction to ammonia, *Appl. Catal., B*, 2020, **265**, 118559–118569.

8 X. Chen, Y. T. Liu, C. Ma, J. Yu and B. Ding, Self-organized growth of flower-like SnS_2 and forest-like ZnS nanoarrays on nickel foam for synergistic superiority in electrochemical ammonia synthesis, *J. Mater. Chem. A*, 2019, **7**, 22235–22241.

9 M. A. Légaré, G. Bélanger-Chabot, R. D. Dewhurst, E. Welz, I. Krummenacher, B. Engels and H. Braunschweig, Nitrogen fixation and reduction at boron, *Science*, 2018, **359**, 896–900.

10 Z. H. Xue, S. N. Zhang, Y. X. Lin, H. Su, G. Y. Zhai, J. T. Han, Q. Y. Yu, X. H. Li, M. Antoniett and J.-S. Chen, Electrochemical education of N_2 into NH_3 by donor-acceptor couples of Ni and Au nanoparticles with a 67.8% faradaic efficiency, *J. Am. Chem. Soc.*, 2019, **141**, 14976–14980.

11 Y. Liu, M. Han, Q. Xiong, S. Zhang, C. Zhao, W. Gong, G. Wang, H. Zhang and H. Zhao, Dramatically enhanced ambient ammonia electrosynthesis performance by in-

operando created Li-S interactions on MoS_2 electrocatalyst, *Adv. Energy Mater.*, 2019, **9**, 1803935.

12 W. Kong, F. Gong, Q. Zhou, G. Yu, L. Ji, X. Sun, A. M. Asiri, T. Wang, Y. Luo and Y. Xu, An MnO_2-$Ti_3C_2T_x$ MXene nanohybrid: an efficient and durable electrocatalyst toward artificial N_2 fixation to NH_3 under ambient conditions, *J. Mater. Chem. A*, 2019, **7**, 18823–18827.

13 X. Wu, L. Xia, Y. Wang, W. Lu, Q. Liu, X. Shi and X. Sun, Mn_3O_4 nanocube: an efficient electrocatalyst toward artificial N_2 fixation to NH_3, *Small*, 2018, **14**, 1803111.

14 X. Zheng, Z. Zhang, X. Li and C. Ding, MnO-carbon nanofiber composite material toward electrochemical N_2 fixation under ambient conditions, *New J. Chem.*, 2019, **43**, 7932–7935.

15 S. Bi, Y. Wu, A. Cao, J. Tian, S. Zhang and Z. Niu, Free-standing three-dimensional carbon nanotubes/amorphous MnO_2 cathodes for aqueous zinc-ion batteries with superior rate performance, *Mater. Today Energy*, 2020, **18**, 100548–100558.

16 H. Tong, T. Li, J. Liu, D. Gong, J. Xiao, L. Shen, B. Ding and X. Zhang, Fabrication of the oxygen vacancy amorphous MnO_2/carbon nanotube as cathode for advanced aqueous zinc-ion batteries, *Energy Technol.*, 2021, **9**, 2000769–2000775.

17 X. Chen, W. Li, Z. Zeng, D. Reed, X. Li and X. Liu, Engineering stable Zn-MnO_2 batteries by synergistic stabilization between the carbon nanofiber core and birnessite-MnO_2 nanosheets shell, *Chem. Eng. J.*, 2021, **405**, 1–12.

18 C. Zhang, B. Anasori, A. Seral-Ascaso, S.-H. Park, N. McEvoy, A. Shmeliov, G. S. Duesberg, J. N. Coleman, Y. Gogotsi and V. Nicolosi, Transparent, flexible, and conductive 2D titanium carbide (MXene) films with high volumetric capacitance, *Adv. Mater.*, 2017, **29**, 1702678.

19 Q. Tang, Z. Zhou and P. Shen, Are MXenes promising anode materials for Li ion batteries? Computational studies on electronic properties and Li storage capability of Ti_3C_2 and $Ti_3C_2X_2$ (X = F, OH) monolayer, *J. Am. Chem. Soc.*, 2012, **134**, 16909–16916.

20 J. Zhao, L. Zhang, X. Xie, X. Li, Y. Ma, Q. Liu, W. H. Fang, X. Shi, G. Cui and X. Sun, $Ti_3C_2T_x$ (T = F, OH) MXene nanosheets: conductive 2D catalysts for ambient electrohydrogenation of N_2 to NH_3, *J. Mater. Chem. A*, 2018, **6**, 24031–24035.

21 T. Li, X. Yan, L. Huang, J. Li, L. Yao, Q. Zhu, W. Wang, W. Abbas, R. Naz, J. Gu, Q. Liu, W. Zhang and D. Zhang, Fluorine-free $Ti_3C_2T_x$ (T = O, OH) nanosheets (50–100 nm) for nitrogen fixation under ambient conditions, *J. Mater. Chem. A*, 2019, **7**, 14462–14465.

22 W. Chen, G. Li, A. Pei, Y. Li, L. Liao, H. Wang, J. Wan, Z. Liang, G. Chen, H. Zhang, J. Wang and Y. Cui, A manganese–hydrogen battery with potential for grid-scale energy storage, *Nat. Energy*, 2018, **3**, 428–437.

23 D. Chao, W. Zhou, C. Ye, Q. Zhang, Y. Chen, L. Gu, K. Davey and S.-Z. Qiao, An electrolytic Zn–MnO_2 battery for high-voltage and scalable energy storage, *Angew. Chem., Int. Ed.*, 2019, **58**, 7823–7828.

24 X. He, H. Guo, T. Liao, Y. Pu, L. Lai, Z. Wang and H. Tang, Electrochemically synthesized SnO_2 with tunable oxygen vacancies for efficient electrocatalytic nitrogen fixation, *Nanoscale*, 2021, **13**, 16307–16315.

25 X. Wang, X. Chi, Z. Fu, Y. Xiong, S. Li, Y. Yao, K. Zhang, Y. Li, S. Wang, R. Zhao, Z. Yang and Y. M. Yan, Interfacial electric field triggered N_2 activation for efficient electrochemical synthesis of ammonia, *Adv. Funct. Mater.*, 2022, **32**, 2202820.

26 M. Liu, Q. Zhao, H. Liu, J. Yang, X. Chen, L. Yang, Y. Cui, W. Huang, W. Zhao, A. Song, Y. Wang, S. Ding, Y. Song, G. Qian, H. Chen and F. Pan, Tuning phase evolution of β-MnO_2 during microwave hydrothermal synthesis for high-performance aqueous Zn ion battery, *Nano Energy*, 2019, **64**, 103942–103948.

27 J. Ye, Z. Yu, W. Chen, Q. Chen and L. Ma, Ionic-liquid mediated synthesis of molybdenumdisulfide/graphene composites: an enhanced electrochemical hydrogen evolution catalyst, *Int. J. Hydrogen Energy*, 2016, **28**, 12049–12061.

28 A. Kafle, D. Gupta, A. Bordoloi and T. C. Nagaiah, Self-standing Fe_3O_4 decorated paper electrode as a binder-free trifunctional electrode for electrochemical ammonia synthesis and Zn-O_2 batteries, *Nanoscale*, 2022, **14**, 16590–16601.

29 X. Fu, J. Zhang and Y. Kang, Recent advances and challenges of electrochemical ammonia synthesis, *Chem Catal.*, 2022, **10**, 2590–2613.

30 M. Han, M. Guo, Y. Yun, Y. Xu, H. Sheng, Y. Chen, Y. Du, K. Ni, Y. Zhu and M. Zhu, Effect of heteroatom and charge reconstruction in atomically precise metal nanoclusters on electrochemical synthesis of ammonia, *Adv. Funct. Mater.*, 2022, **32**, 2202820.

31 C. Wang, X. Zhua and P. Zuo, Novel confinement of Mn_3O_4 nanoparticles on two-dimensional carbide enabling high-performance electrochemical synthesis of ammonia under ambient conditions, *Chem. Eng. J.*, 2020, **396**, 125163.

32 A. Liu, Q. Yang, X. Ren, M. Gao, Y. Yang, L. Gao, Y. Li, Y. Zhao, X. Liang and T. Ma, Two-dimensional CuAg/Ti_3C_2 catalyst for electrochemical synthesis of ammonia under ambient conditions: a combined experimental and theoretical study, *Sustainable Energy Fuels*, 2020, **4**, 5061–5071.

33 K. P. Ramaiyan, S. Ozden, S. Maurya, D. Kelly, S. K. Babu, A. Benavidez, F. G. Garzon, Y. S. Kim, C. R. Kreller and R. Mukundan, Molybdenum carbide electrocatalysts for electrochemical synthesis of ammonia from nitrogen: activity and stability, *J. Electrochem. Soc.*, 2020, **167**, 044506.

34 Z. Wang, Z. Dai, H. Yu, H. Zhang, W. Tian, Y. Xu, X. Li, L. Wang and H. Wang, Pore-size-tuned Pd films grown on Ni foam as an advanced catalyst for electrosynthesis of ammonia, *ACS Sustainable Chem. Eng.*, 2020, **31**, 11827–11833.

35 X. He, H. Guo, T. Liao, Y. Pu, L. Lai, Z. Wang and H. Tang, Electrochemically synthesized SnO_2 with tunable oxygen vacancies for efficient electrocatalytic nitrogen fixation, *Nanoscale*, 2021, **13**, 16307–16315.

36 Y. Wang, M. Batmunkh, H. Mao, H. Li, B. Jia, S. Wu, D. Liu, X. Song, Y. Sun and T. Ma, Low-overpotential electrochemical ammonia synthesis using BiOCl-modified 2D titanium carbide MXene, *Chin. Chem. Lett.*, 2022, **33**, 394–398.

37 M. Sun, C. Ma, M. Ma, Y. Wei, S. Dong, X. Zhang, J. Tian and M. Shao, Electrochemical ammonia synthesis *via* nitrogen reduction reaction on 1T/2H mixed-phase MoSSe catalyst: Theoretical and experimental studies, *Mater. Today Phys.*, 2023, **30**, 100945.

38 L. Tan, N. Yang, X. Huang, L. Peng, C. Tong, M. Deng, X. Tang, L. Li, Q. Liao and Z. Wei, Synthesis of ammonia *via* electrochemical nitrogen reduction on high-index faceted Au nanoparticles with a high faradaic efficiency, *Chem. Commun.*, 2019, **55**, 14482.

39 M. Wang, S. Liu, T. Qian, J. Liu, J. Zhou, H. Ji, J. Xiong, J. Zhong and C. Yan, Over 56.55% Faradaic efficiency of ambient ammonia synthesis enabled by positively shifting the reaction potential, *Nat. Commun.*, 2019, **10**, 341.